Electronic Supplementary Information (ESI) for

# Increased Humidity Can Soften Glassy Langmuir Polymer Films by Two Mechanisms: Plasticization of the Polymer Material, and Suppression of the Evaporation Cooling Effect

***Hyun Chang Kim[a], Yun Hwa Choi[a], Wei Bu[b], Mati Meron[b], Binhua Lin[b], You-Yeon Won[a]****

[a]School of Chemical Engineering, Purdue University, West Lafayette, Indiana 47907

[b]Advanced Photon Source, University of Chicago, Chicago, Illinois 60439

* To whom correspondence should be addressed. E-mail: yywon@ecn.purdue.edu

## S1. Estimation of the Surface Temperature of Water ($T_{surface}$) under the Influence of Continuous Evaporation of the Water

The surface temperature of water was estimated by solving the energy balance equation for the region near the air-water interface. In our typical experimental situation, the bulk temperature of the water ($T_{water}$ = 25 °C) is higher than the bulk temperature of the air ($T_{air}$ = 22 °C), so there is a continuous heat transfer from water to air across the interface. The interface continuously exchanges heat with the bulk water and air phases. These heat transfer processes occur by buoyancy-driven free convection in both the water and air phases; the associated heat fluxes will be denoted as $q_{water}$ and $q_{air}$, respectively. Across the air-water interface, phase transition/mass transfer (water evaporation) occurs, which itself is an endothermic process; the heat flux due to evaporation at the air-water interface will be denoted as $Q_{evap}$. The surface temperature of water was calculated in the following steps. (i) $q_{water}$ was calculated as a function of $T_{surface}$ at fixed $T_{water}$. (ii) $q_{air}$ was calculated as a function of $T_{surface}$ at fixed $T_{air}$. (iii) For a given RH level, $Q_{evap}$ was calculated as a function of $T_{surface}$ at fixed $T_{air}$. (iv) At steady state the total heat fluxes across the air-water interface should be balanced:

$$q_{water} = q_{air} + Q_{evap}. \qquad \text{(S1)}$$

This total energy balance for the air-water interface was solved to calculate $T_{surface}$ for each different RH (as demonstrated in Figure S1 below). The details of the calculations are given below.

### (1) Heat Transfer due to Free Convection in the Bulk Water and Air Phases ($q_{water}$ and $q_{air}$, Respectively)

The convective heat fluxes on the water and air sides of the interface ($q_{water}$ and $q_{air}$, respectively) were calculated using the "Newton's law of cooling"

$$q_{water} = h_{water} \cdot \left(T_{water} - T_{Surface}\right) \qquad \text{(S2)}$$

$$q_{air} = h_{air} \cdot \left(T_{surface} - T_{air}\right) \qquad \text{(S3)}$$

where $h_{water}$ and $h_{air}$ are the heat transfer coefficients of the water and air, respectively; note these heat transfer coefficients take into account both conductive and convective contributions to heat transfer. The values of these heat transfer coefficients were estimated from empirical correlations of the respective Nusselt numbers, $Nu_{water}$ and $Nu_{air}$, as explained in the next paragraph. The bulk water temperature, $T_{water}$, was measured using a waterproof thermocouple placed at 0.01 m depth beneath the water surface. The bulk air temperature, $T_{air}$, was measured (along with RH) using an NIST-certified digital thermometer located at 0.08 m above the water surface. At various assumed values of water surface temperature ($T_{surface}$), the values of $h_{water}$ and $h_{air}$ were estimated.

For free convection systems, it can be shown by dimensional analysis that the dimensionless heat transfer coefficient, Nusselt number ($Nu \equiv hL/k$), depends on the heat transfer Grashof number ($Gr_h$), the Prandtl number ($Pr$), and the characteristic length ($L$).[1] In our experimental situation, the maximum values of $Gr_h \cdot Pr$ were estimated to be 9.3 × $10^6$ for water at $\Delta T$ ($\equiv T_{water} - T_{Surface}$) = 3 °C, and 6.8 × $10^4$ for air at $\Delta T$ ($\equiv T_{surface} - T_{air}$) = 3 °C, which suggests that the flow is predominantly laminar, and the turbulent effect is insignificant (as confirmed below). The mean Nusselt number for laminar flow

($Nu^{lam}$), the mean Nusselt number for turbulent flow ($Nu^{turb}$), and the total mean Nusselt number ($Nu$) were estimated using established empirical relationships[1]

$$Nu^{lam} = \frac{1.4}{\ln(1+\frac{1.4}{0.835\cdot\overline{C_l}(Pr)(Gr\cdot Pr)^{1/4}})} \quad \text{(S4)}$$

$$Nu^{turb} = 0.14 \cdot \frac{1+0.0107\cdot Pr}{1+0.01\cdot Pr}(Gr\cdot \mathrm{Pr})^{1/3} \quad \text{(S5)}$$

$$Nu = [(Nu^{lam})^{10} + (Nu^{turb})^{10}]^{1/10}. \quad \text{(S6)}$$

In these calculations, the ratio of the area to the perimeter of the Langmuir trough was used as the characteristic length scale ($L = A/P$). The empirical function, $\overline{C_l}(Pr)$, is given by

$$\overline{C_l}(Pr) = \frac{0.671}{\left[1+(0.492/Pr)^{9/16}\right]^{4/9}}. \quad \text{(S6)}$$

For water, for instance, at $\Delta T$ ($\equiv T_{water} - T_{Surface}$) = 3 °C (at $Gr_h{\cdot}Pr$ = 9.3 × 10$^6$), $Nu^{lam}$, $Nu^{turb}$ and $Nu$ were estimated to be 28.82, 1.09 and 28.82, respectively, which confirms that the turbulent correction is indeed negligible.

**(2) Heat Flux due to Phase Transition/Mass Transfer (Water Evaporation) across the Air-Water Interface ($Q_{evap}$)**

The heat flux due to evaporation at the air-water interface ($Q_{evap}$) was calculated by

$$Q_{evap} = \dot{m}_{evap} \cdot \Delta H_{vap} \quad \text{(S7)}$$

where $\dot{m}_{evap}$ is the evaporation mass flux, and $\Delta H_{vap}$ is the heat of vaporization of water per mass of water; the temperature dependence of $\Delta H_{vap}$ was estimated using the data reported in Ref. 2. The evaporation flux, $\dot{m}_{evap}$, was calculated using the relation,

$$\dot{m}_{evap} = h_{evap} \cdot \Delta\rho_{wv} \quad \text{(S8)}$$

where $h_{evap}$ is the evaporation mass transfer coefficient, and $\Delta\rho_{wv}$ is the density difference between the saturated water vapor at the air-water interface ($\rho_{wv}^{sat}(T_{surface})$) and the water vapor in the bulk air ($RH \cdot \rho_{wv}^{sat}(T_{air})$), $\Delta\rho_{wv} = \rho_{wv}^{sat}(T_{surface}) - RH \cdot \rho_{wv}^{sat}(T_{air})$; these temperature-dependent saturated water vapor density values were obtained from Ref. 3. The mass transfer coefficient was estimated from an empirical correlation of the Sherwood number ($Sh \equiv h_{evap}L/D$ where $L = A/P$, and $D$ is the temperature-dependent binary diffusion coefficient of water vapor in air) for laminar free convection[4]

$$Sh = 0.54 \cdot (Gr_m \cdot Sc)^{1/4} \quad \text{(S9)}$$

where $Gr_m$ is the mass transfer Grashof number, and $Sc$ is the Schmidt number; in calculating the values of $Gr_m$, the temperature-dependent saturated water vapor pressure was estimated using the method reported in Ref. 5. The above equation is valid only in the laminar, free convection evaporation regime (that is, when $Gr_m{\cdot}\, Sc$ < 2 × 10$^7$). In our situation, the maximum value of $Gr_m{\cdot}\, Sc$ was estimated to be 1.5 × 10$^5$ at $\Delta T$ ($\equiv T_{surface} - T_{air}$) = 3 °C and RH = 0%, which justifies the use of the above equation.

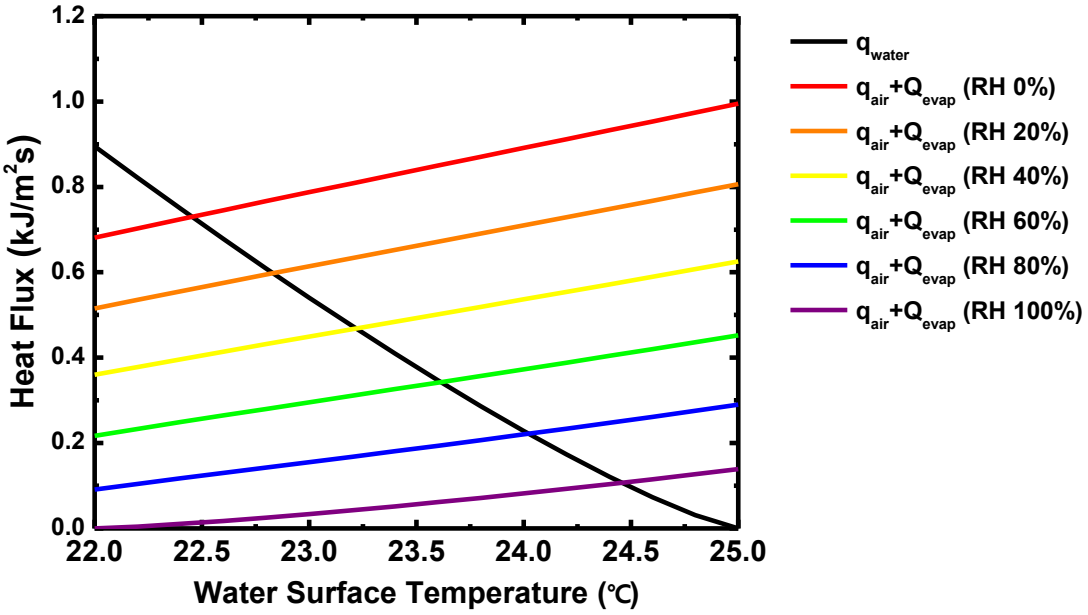


**Figure S1.** Heat fluxes on the water and air sides of the interface ($q_{water}$ and $q_{air} + Q_{evap}$, respectively) estimated at various assumed values of water surface temperature ($T_{surface}$) and relative humidity (RH).

**S2. Box-Model Analysis of the X-ray Reflectivity Data**

A detailed explanation of the analysis method used can be found in our previous publication [Lee et al., *Soft Matter*, 10, 3771 (2014)]. Briefly, to convert the X-ray reflectivity (XR) profiles to real-space electron density profiles, the so-called box-model analysis method was used. The raw XR data were first shifted horizontally by adding an offset ($q_{z,offset}$), and then vertically by multiplying the reflectivity data ($R(q_z)$) by a constant ($R_{shift}$):

$$q_z = q_{z,original} + q_{z,offset} \quad \text{(S6)}$$

$$R(q_z) = R_{original}(q_z) \times R_{shift}. \quad \text{(S7)}$$

This corrected reflectivity profile was then normalized by the theoretical Fresnel reflectivity profile:

$$R_F(q_z) = \left| \frac{q_z - \sqrt{q_z^2 - q_c^2 - 4ik\mu}}{q_z + \sqrt{q_z^2 - q_c^2 - 4ik\mu}} \right|^2 . \quad \text{(S8)}$$

The box-model fitting analysis was performed on this normalized data ($R(q_z)/R_F(q_z)$). We assumed that the monolayer is composed of four sublayers (i.e., "boxes") of variable thickness ($\mathbf{d_1}$, $\mathbf{d_2}$, $\mathbf{d_3}$, $\mathbf{d_4}$) and electron density ($\boldsymbol{\rho_{e,1}}$, $\boldsymbol{\rho_{e,2}}$, $\boldsymbol{\rho_{e,3}}$, $\boldsymbol{\rho_{e,4}}$), each bounded by error function-type interfaces of variable roughness ($\boldsymbol{\sigma_1}$, $\boldsymbol{\sigma_2}$, $\boldsymbol{\sigma_3}$, $\boldsymbol{\sigma_4}$, $\boldsymbol{\sigma_5}$):

$$\rho_e(z) = \frac{(\rho_{e,1} - \rho_{e,air})}{2}\left(1 + \mathrm{erf}\left(\frac{z}{\sqrt{2\sigma_1^2}}\right)\right) + \frac{(\rho_{e,2} - \rho_{e,1})}{2}\left(1 + \mathrm{erf}\left(\frac{z - d_1}{\sqrt{2\sigma_2^2}}\right)\right) + \frac{(\rho_{e,3} - \rho_{e,2})}{2}\left(1 + \mathrm{erf}\left(\frac{z - (d_1 + d_2)}{\sqrt{2\sigma_3^2}}\right)\right) + \frac{(\rho_{e,4} - \rho_{e,3})}{2}\left(1 + \mathrm{erf}\left(\frac{z - (d_1 + d_2 + d_3)}{\sqrt{2\sigma_4^2}}\right)\right) + \frac{(\rho_{e,sub} - \rho_{e,4})}{2}\left(1 + \mathrm{erf}\left(\frac{z - (d_1 + d_2 + d_3 + d_4)}{\sqrt{2\sigma_5^2}}\right)\right). \quad \text{(S9)}$$

The assumed electron density profile calculated using Equation (S9) was converted through the first Born approximation to an expected XR profile. Then this predicted XR profile was compared with the experimental data. This process was repeated to find the thickness, electron density and roughness values that minimize the sum of the magnitudes of the differences between the measured and calculated XR values at all the data points:

$$\varepsilon = \sum_{i=1}^{N} \left( \frac{\left| R_{experiment,i}(q_z) - R_{calculation,i}(q_z) \right|}{R_{F,i}(q_z)} \right). \quad \text{(S10)}$$

**Table S1.** Box model fit parameters for the normalized electron density profiles of Langmuir PLGA films at 50 – 60 % RH. The actual reflectivity data are presented in Figure S2. The notations, $\mathbf{d_i}$, $\boldsymbol{\rho_{e,i}}$, and $\boldsymbol{\sigma_i}$, denote the thickness, electron density and roughness of the i-th sublayer (or interface) within the monolayer, respectively**.** The subscript value "1" corresponds to the sublayer (or interface) closest to the bulk air phase, and the highest subscript number designates the sublayer (or interface) closest to the bulk water.

| Beamtime Run | Area Per Chain ($Å^2$) | $\mathbf{d_1}$ (Å) | $\mathbf{d_2}$ (Å) | $\mathbf{d_3}$ (Å) | $\mathbf{d_4}$ (Å) | $\boldsymbol{\rho_{e,1}/\rho_{e,water,\infty}}$ | $\boldsymbol{\rho_{e,2}/\rho_{e,water,\infty}}$ | $\boldsymbol{\rho_{e,3}/\rho_{e,water,\infty}}$ | $\boldsymbol{\rho_{e,4}/\rho_{e,water,\infty}}$ | $\boldsymbol{\sigma_1}$ (Å) | $\boldsymbol{\sigma_2}$ (Å) | $\boldsymbol{\sigma_3}$ (Å) | $\boldsymbol{\sigma_4}$ (Å) | $\boldsymbol{\sigma_5}$ (Å) |
|---|---|---|---|---|---|---|---|---|---|---|---|---|---|---|
| 201407 | **2028-3** | 10.0398 | 18.5362 | 10.4509 | 15.7988 | 1.17606 | 1.32267 | 1.10375 | 0.968832 | 2.73997 | 3.11182 | 5.79648 | 6.97946 | 8.22898 |
| | **2028-2** | 10.348 | 18.7572 | 10.3605 | 15.7953 | 1.19066 | 1.32325 | 1.11387 | 0.959309 | 2.77601 | 2.83181 | 5.74784 | 7.22253 | 8.11515 |
| | **2028-1** | 7.35422 | 11.0605 | 15.2622 | 19.3704 | 1.08411 | 1.31973 | 1.37452 | 0.936438 | 2.43394 | 3.72745 | 4.84312 | 9.70332 | 9.71692 |
| | **701-3** | 6.06457 | 5.21968 | 46.1485 | 28.1245 | 1.08682 | 1.25792 | 1.31694 | 1.26146 | 2.41205 | 1.60854 | 2.97611 | 9.95445 | 4.64131 |
| | **701-2** | 5.44676 | 3.93966 | 49.842 | 25.6271 | 1.10599 | 1.22546 | 1.32029 | 1.26786 | 2.5508 | 1.70906 | 3.12405 | 11.1852 | 4.59744 |
| | **701-1** | 5.08691 | 3.6105 | 49.3873 | 26.5288 | 1.10798 | 1.2164 | 1.33095 | 1.2581 | 2.55737 | 1.87685 | 3.01363 | 11.896 | 4.46938 |
| 201502 | **2028-3** | 12.2103 | 15.9581 | 14.2155 | 16.4723 | 1.36166 | 1.24467 | 1.04405 | 0.978791 | 2.67931 | 4.51571 | 7.82402 | 7.17232 | 8.11795 |
| | **2028-2** | 12.2894 | 16.4188 | 14.0231 | 16.1943 | 1.35701 | 1.23888 | 1.03894 | 0.97792 | 2.68117 | 4.7874 | 7.65039 | 7.12475 | 7.89844 |
| | **2028-1** | 12.8123 | 11.4014 | 9.63064 | 9.90376 | 1.34366 | 1.24438 | 1.1418 | 1.03037 | 2.65369 | 3.9023 | 4.4645 | 4.69395 | 3.82712 |
| | **701-3** | 5.41356 | 14.1021 | 35.0698 | 25.5246 | 1.14451 | 1.31543 | 1.28672 | 1.24187 | 2.63885 | 3.745 | 31.3893 | 4.49199 | 5.20714 |
| | **701-2** | 5.57185 | 14.566 | 35.0426 | 24.9328 | 1.1562 | 1.32856 | 1.27994 | 1.24599 | 2.67774 | 4.3513 | 26.6785 | 4.03915 | 5.08683 |
| | **701-1** | 6.35766 | 14.0054 | 35.2304 | 25.9348 | 1.12452 | 1.32009 | 1.30571 | 1.25706 | 2.66504 | 4.31512 | 12.788 | 8.91892 | 4.80589 |

**Figure S2.** Normalized XR profiles ($R(q_z)/R_F(q_z)$) from Langmuir PLGA films at 50 – 60 % RH and at two different area per chain conditions, 2028 and 701 $Å^2$/chain. At each area condition, three different areas of the monolayer were examined. These measurements were repeated twice in two different beam times (first in July 2014, and again in February 2015). Points are experimental data. Solid lines are theoretical fits to the data. The procedures for this box-model fitting analysis are described in Section S2 of the SI. The normalized electron density profiles ($\rho_e(z)/\rho_{e,water,\infty}$) obtained from this analysis are presented in Figure 8(c) of the main text. The values of the best-fit parameters are presented in Table S1 of the ESI.

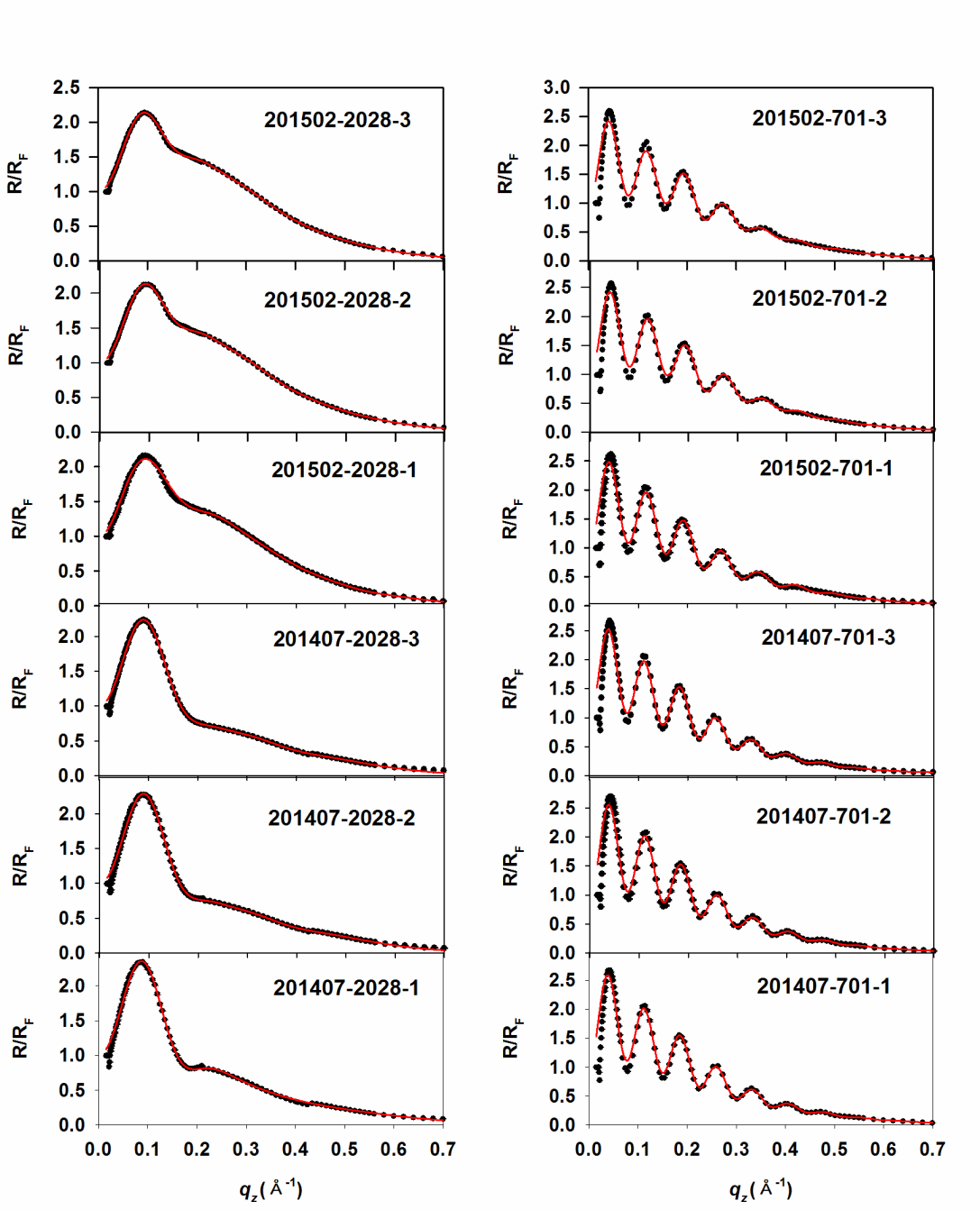

**Table S2.** Box model fit parameters for the normalized electron density profiles of Langmuir PLGA films at 80 – 90 % RH. The actual reflectivity data are presented in Figure S3. The notations, $\mathbf{d_i}$, $\boldsymbol{\rho_{e,i}}$, and $\boldsymbol{\sigma_i}$, denote the thickness, electron density and roughness of the i-th sublayer (or interface) within the monolayer, respectively**.** The subscript value "1" corresponds to the sublayer (or interface) closest to the bulk air phase, and the highest subscript number designates the sublayer (or interface) closest to the bulk water.

| Beamtime Run | Area Per Chain (Å$^2$) | $\mathbf{d_1}$ (Å) | $\mathbf{d_2}$ (Å) | $\mathbf{d_3}$ (Å) | $\mathbf{d_4}$ (Å) | $\boldsymbol{\rho_{e,1}/\rho_{e,water,\infty}}$ | $\boldsymbol{\rho_{e,2}/\rho_{e,water,\infty}}$ | $\boldsymbol{\rho_{e,3}/\rho_{e,water,\infty}}$ | $\boldsymbol{\rho_{e,4}/\rho_{e,water,\infty}}$ | $\boldsymbol{\sigma_1}$ (Å) | $\boldsymbol{\sigma_2}$ (Å) | $\boldsymbol{\sigma_3}$ (Å) | $\boldsymbol{\sigma_4}$ (Å) | $\boldsymbol{\sigma_5}$ (Å) |
|---|---|---|---|---|---|---|---|---|---|---|---|---|---|---|
| 201407 | **2028-3** | 7.70877 | 11.0291 | 12.4248 | 17.217 | 1.09038 | 1.32334 | 1.339130 | 0.961611 | 2.55931 | 3.37799 | 5.06408 | 8.55437 | 8.74779 |
| | **2028-2** | 7.70877 | 11.0291 | 12.4248 | 17.217 | 1.09038 | 1.32334 | 1.339130 | 0.96161 | 2.55931 | 3.37798 | 5.06408 | 8.55437 | 8.74779 |
| | **2028-1** | 7.51424 | 10.6292 | 12.2998 | 17.3311 | 1.07608 | 1.33624 | 1.357350 | 0.962604 | 2.5116 | 3.48622 | 5.05737 | 8.50635 | 8.82553 |
| | **701-3** | 6.03289 | 5.14703 | 49.5774 | 26.7454 | 1.03962 | 1.25378 | 1.319210 | 1.260050 | 2.34665 | 1.57145 | 2.91981 | 11.6993 | 4.77285 |
| | **701-2** | 6.02524 | 5.13628 | 49.847 | 26.6282 | 1.04546 | 1.25290 | 1.320810 | 1.262500 | 2.34056 | 1.30107 | 2.70693 | 12.8515 | 4.70793 |
| | **701-1** | 6.05728 | 5.33529 | 49.6038 | 26.9074 | 1.03738 | 1.25743 | 1.326030 | 1.258230 | 2.35519 | 1.59540 | 3.09696 | 12.5536 | 4.57802 |
| 201502 | **2028-3** | 6.92524 | 12.2564 | 11.1080 | 15.0275 | 1.21168 | 1.29671 | 1.252490 | 0.984788 | 2.63538 | 3.73771 | 6.4701 | 7.89086 | 8.03567 |
| | **2028-2** | 6.52484 | 10.3898 | 13.0082 | 14.3495 | 1.23481 | 1.29844 | 1.216390 | 0.988855 | 2.63319 | 3.49671 | 6.48184 | 7.44533 | 7.63680 |
| | **2028-1** | 9.78381 | 18.8869 | 18.3571 | 9.62387 | 1.25724 | 1.30081 | 0.987851 | 0.986087 | 2.76743 | 1.48552 | 8.03054 | 2.97948 | 5.58281 |
| | **701-3** | 8.46016 | 21.4094 | 20.297 | 25.7376 | 1.22127 | 1.30402 | 1.308220 | 1.246910 | 3.04055 | 2.72902 | 16.9705 | 12.7558 | 5.22045 |
| | **701-2** | 8.70576 | 21.5392 | 20.6628 | 26.3867 | 1.22464 | 1.30136 | 1.324520 | 1.257970 | 2.99156 | 2.65345 | 16.5254 | 12.6354 | 5.01654 |
| | **701-1** | 9.48164 | 20.0934 | 20.7265 | 27.0900 | 1.23199 | 1.31487 | 1.312600 | 1.257020 | 3.01954 | 2.56598 | 16.385 | 13.2735 | 4.51972 |

**Figure S3.** Normalized XR profiles ($R(q_z)/R_F(q_z)$) from Langmuir PLGA films at 80 – 90 % RH and at two different area per chain conditions, 2028 and 701 $Å^2$/chain. At each area condition, three different areas of the monolayer were examined. These measurements were repeated twice in two different beam times (first in July 2014, and again in February 2015). Points are experimental data. Solid lines are theoretical fits to the data. The procedures for this box-model fitting analysis are described in Section S2 of the SI. The normalized electron density profiles ($\rho_e(z)/\rho_{e,water,\infty}$) obtained from this analysis are presented in Figure 8(c) of the main text. The values of the best-fit parameters are presented in Table S2 of the ESI.

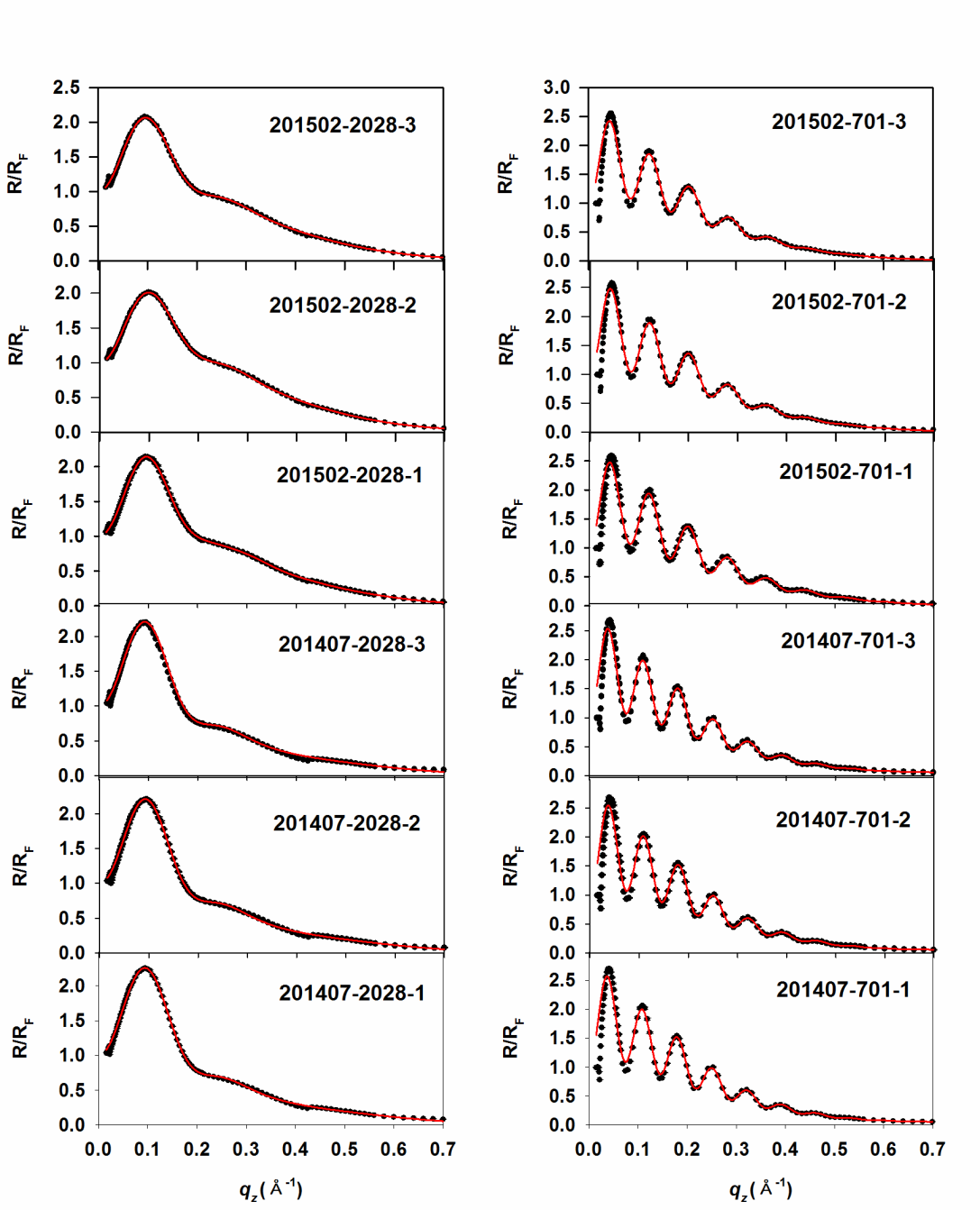

**S3. Correction of Surface Pressure for Non-Zero Contact Angle**

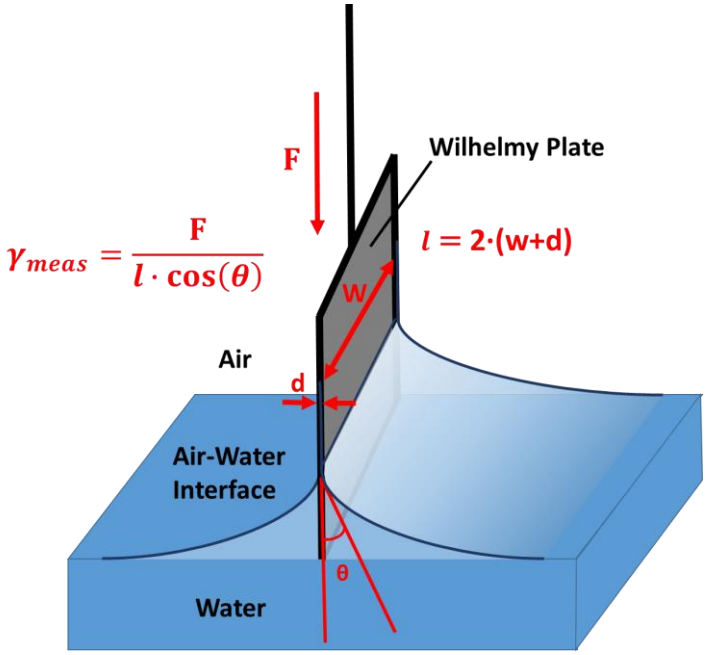


**Figure S4.** Schematic illustration of the Wilhelmy method.

In a typical Wilhemly plate setup, the surface pressure ($\pi_{meas}$) is related to the capillary force ($F$) and the contact angle ($\theta$) by the Wilhelmy equation

$$\pi_{meas} = \gamma_{air-water} - \gamma_{meas} = \gamma_{air-water} - \frac{F}{l \cdot \cos(\theta)} \qquad \text{(S11)}$$

Here $\theta$ is assumed to be zero, which gives

$$\pi_{meas} = \gamma_{air-water} - \frac{F}{l}; \qquad \gamma_{meas} = -\frac{F}{l}. \qquad \text{(S12)}$$

If $\theta$ is not zero, the true surface pressure ($\pi_{ture}$) is different from $\pi_{meas}$, and can be estimated from the measured contact angle ($\theta_{meas}$). The Wilhelmy equation gives

$$\pi_{true} = \gamma_{air-water} - \gamma_{true} = \gamma_{air-water} - \frac{F}{l \cdot \cos(\theta_{meas})}. \qquad \text{(S13)}$$

By removing $F$ using Equation (S12), we obtain

$$\pi_{true} = \gamma_{air-water} - \frac{\gamma_{meas} \cdot l}{l \cdot \cos(\theta_{meas})}, \qquad \text{(S14)}$$

which becomes

$$\pi_{true} = \gamma_{air-water} - \gamma_{meas} \cdot \sec(\theta_{meas}). \qquad \text{(S15)}$$

Therefore, $\pi_{true}$ can be calculated from $\gamma_{meas}$ and $\theta_{meas}$.

The error in surface pressure as defined in Section 3.5 of the main text

$$\Delta\pi = \pi_{meas} - \pi_{true} \qquad \text{(S16)}$$

can thus be calculated as

$$\Delta\pi = (\gamma_{air-water} - \pi_{meas}) \cdot (\sec(\theta_{meas}) - 1). \qquad \text{(S18)}$$

**Figure S5.** Optical images of **(a)** the platinum Wilhelmy plate in contact with the Langmuir PnPMA film at 30 – 40 % RH and a surface pressure of 10.24 mN/m, and **(b)** the filter paper Wilhelmy probe in contact with the Langmuir PnPMA film at 30 - 40 % RH and a surface pressure of 10.01 mN/m. The images were taken using a digital camera and analyzed with the ImageJ software for the determination of the contact angle.

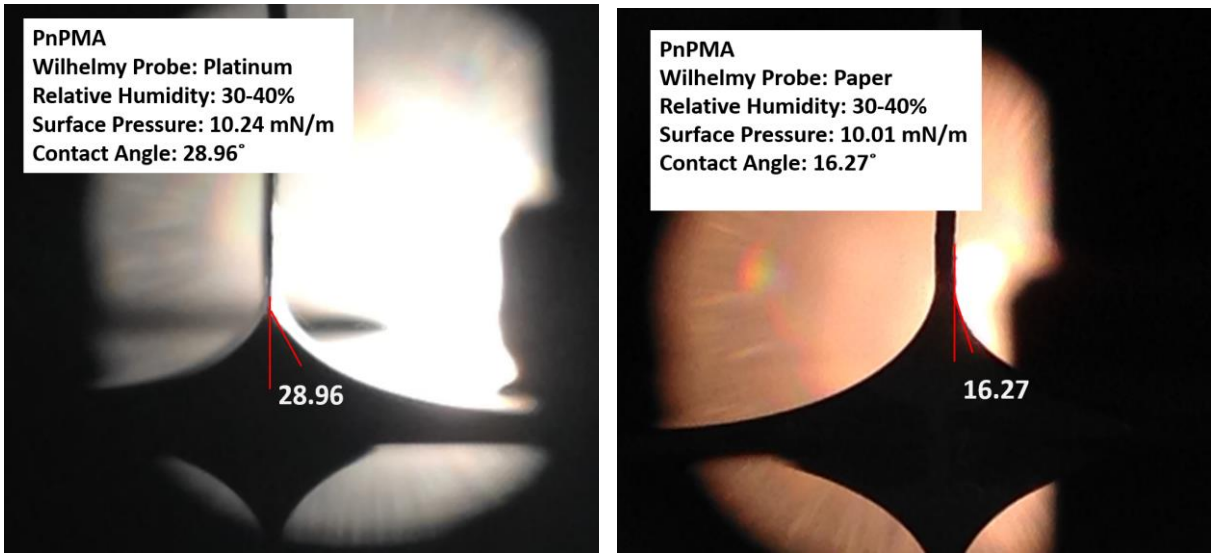

**Figure S6.** Optical images of **(a)** the platinum Wilhelmy plate in contact with a clean air-water interface at 40 – 5- RH, and **(b)** the filter paper Wilhelmy probe in contact with a clean air-water interface at 40 – 50 % RH. The images were taken using a digital camera and analyzed with the ImageJ software for the determination of the contact angle.

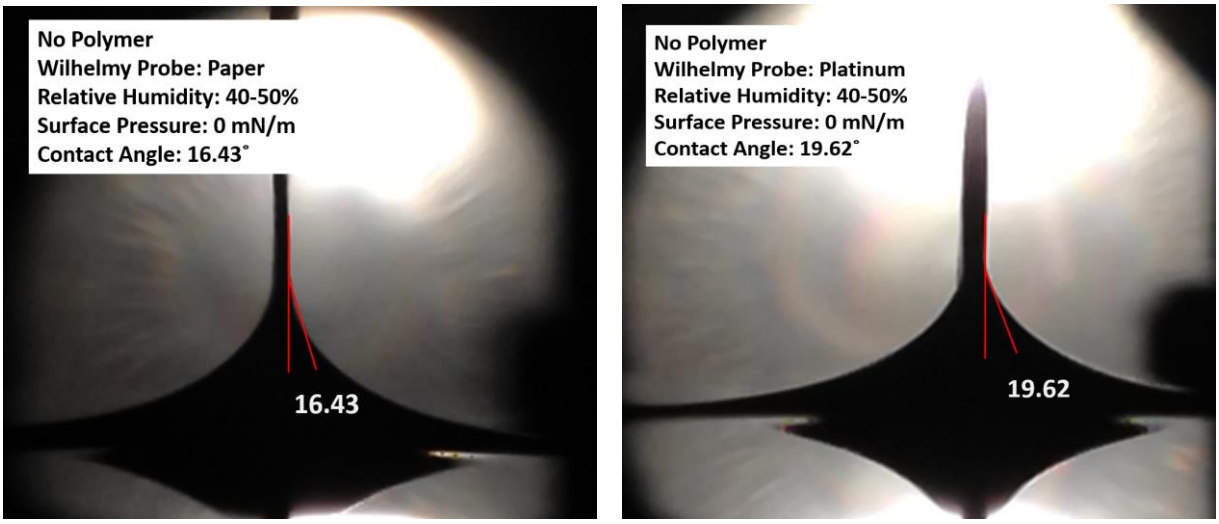

**References for ESI**


1. R. B. Bird, W. E. Stewart, E. N. Lightfoot and D. J. Klingenberg, *Introductory Transport Phenomena*, Wiley, 2015.
2. K. N. Marsh, ed., *Recommended Reference Materials for the Realization of Physicochemical Properties*, Blackwell, Oxford, UK, 1987.
3. R. Nave, Empirical Fit of Saturated Vapor Density versus Celsius Temperature, http://hyperphysics.phy-astr.gsu.edu/hbase/Kinetic/relhum.html#c3, Accessed March 29, 2017.
4. M. T. Pauken, *Experimental Thermal and Fluid Science*, 1998, **18**, 334-340.
5. A. L. Buck, *Journal of Applied Meteorology*, 1981, **20**, 1527-1532.